

Behavior and modeling of superelastic shape memory alloy reinforced concrete beams



Alaa Abdulridha^a, Dan Palermo^{a,*}, Simon Foo^b, Frank J. Vecchio^c

^a Dept. of Civil Engineering, University of Ottawa, 161 Louis Pasteur St., Ottawa, ON, Canada K1N 6N5

^b Real Property Branch, Public Works and Government Services Canada, Gatineau, QC, Canada

^c Dept. of Civil Engineering, University of Toronto, 35 St. George St., Toronto, ON, Canada M5S 1A4

ARTICLE INFO

Article history:

Received 22 December 2011

Revised 28 December 2012

Accepted 29 December 2012

Keywords:

Superelastic SMA
Reinforced concrete beams
Strain recovery
Cyclic loading
Energy dissipation
Hysteretic response
Constitutive modeling
Finite element analysis

ABSTRACT

The re-centering phenomenon of superelastic Shape Memory Alloy (SMA) reinforced concrete is a unique characteristic that is appealing for structural applications, along with the ability to respond with stable hystereses and achieve similar strength and ductility to concrete reinforced with conventional deformed bars. The objective of this study was to investigate the structural performance of superelastic SMA reinforced concrete and to develop a preliminary constitutive model applicable to nonlinear finite element algorithms. Seven simply supported flexure-critical concrete beams, reinforced with either SMA bars in the critical region or conventional deformed reinforcement, were subjected to monotonic, cyclic, and reverse cyclic loading. The experiment results demonstrated the superior capacity of the SMA beams to recover inelastic displacements. The SMA beams sustained displacement ductility and strength capacity comparable to the conventional beams. Crack widths and crack spacing were larger in the SMA beams; however, upon removal of load, the crack openings were recovered. Energy dissipation was lower in the SMA beams, particularly when subjected to reverse cyclic loading. The constitutive model based on a trilinear backbone envelope response and linear unloading and reloading rules provided satisfactory simulations.

© 2013 Elsevier Ltd. All rights reserved.

1. Introduction

Concrete structures subjected to rare loading events, including blasts, impacts, and earthquakes, are expected, in many situations, to respond in the inelastic range and suffer permanent damage. As an example, the primary objective in seismic design is to ensure life safety and prevent structural collapse during a major earthquake. For concrete structures located in high seismic regions this is typically achieved through the formation of well-defined plastic hinges, resulting in damage due to permanent straining in the reinforcement and permanent deformations in the structural members. While the main objective may be achieved, the sustained damage could prevent the structure from being serviceable and prohibit post-earthquake repairs.

Recently, a new group of alloys known as Shape Memory Alloys (SMAs) has emerged in the research community. Shape memory alloys have the ability to sustain large deformations; however, they return to their original undeformed shape upon removal of stress (superelastic SMA) or with the application of heat (shape memory effect). In addition, SMAs can dissipate energy through hysteretic damping and be heat-treated to attain comparable strength to

conventional deformed reinforcement. The unique properties of SMAs can address some of the shortcomings of conventional deformed reinforcing bars; specifically by controlling permanent strains. Although SMAs possess characteristics that make them appealing for structural applications, there are some disadvantages, including: high cost, which leads to optimization of the material and the use of mechanical couplers to connect to conventional steel; difficulty in machining the material; the dependency of the superelastic properties on operating temperature; the smooth bar surface, which reduces the bond to surrounding concrete resulting in larger crack widths; and the low elastic modulus that can result in larger displacements under service loads. Nickel–Titanium (NiTi), consisting of approximately 56% nickel and 44% titanium alloy, is the most common type of SMA investigated for structural applications. Nitinol is the term frequently used for nickel–titanium SMA.

A number of studies have focused on material characterization and mechanical properties of superelastic NiTi bars and wires to evaluate the material for use in structural applications. DesRoches et al. [1] demonstrated that SMA in wire form experienced higher strength and damping properties compared to SMA bars; however, the re-centering capabilities based on residual strains were not affected by the form of the SMA. A study by Tyber et al. [2] on large diameter NiTi bars revealed that transformation temperatures and

* Corresponding author. Tel.: +1 613 562 5800x6141; fax: +1 613 562 5173.

E-mail address: palermo@eng.uottawa.ca (D. Palermo).

Nomenclature

A_s	area of flexural reinforcement	f_{unt}	unloading plateau stress of reinforcement
E_c	initial tangent modulus of elasticity of concrete	f_y	yield stress of reinforcement
E_i	initial modulus of elasticity of reinforcement	Δ	displacement
E_{sh}	strain hardening modulus of reinforcement	Δ_y	yield displacement
E_s	modulus of elasticity of reinforcement	ε_c	strain at peak concrete cylinder compressive stress
P	load	ε_m	current maximum strain of reinforcement
P_y	yield load	ε_p	plastic offset strain of reinforcement
R_{cr}	residual crack width	ε_{r1}	first unloading strain
S_{cr}	crack spacing	ε_{r2}	second unloading strain
W_{cr}	maximum crack width	ε_s	current reinforcement strain
f_c	concrete cylinder compressive strength	ε_{s-i}	reinforcement strain from the previous load step
f_m	current maximum stress of reinforcement	ε_{sh}	the strain at the onset of strain hardening
f_s	current reinforcement stress	ε_u	ultimate strain of reinforcement
f_{s-i}	reinforcement stress from the previous load step	ε_y	yield strain of reinforcement
f_u	ultimate stress of reinforcement		

hardness depended on bar heat treatment and not bar diameter. McCormick et al. [3] studied the deformation behavior of large diameter superelastic bars, which confirmed that the re-centering capability and equivalent viscous damping increased with a decrease in bar size. Dolce and Cardone [4] were able to show that NiTi shape memory alloy wires are suitable as kernel components for seismic protection devices, specifically owing to the re-centering and energy dissipation characteristics. Others studies have focused on a wide range of use for SMAs [5–7], including reinforcement in new construction or for repair and retrofitting of existing structural elements, and as strands for prestressing and post-tensioning. SMA-based devices for passive, semi-active or active control of structures, including kernel components for dampers and isolators, are other possible uses.

Experimental research involving SMAs in concrete structures is limited and has generally been directed toward new construction. This includes exploratory research on small-scale beams reinforced with either embedded or externally anchored SMAs [8,9], and the seismic behavior of columns reinforced with SMA bars and engineered cementitious concrete in the plastic hinge region as a technique to reduce damage [10,11]. Other studies have included the use of SMA embedded bars in beam–column joints [12], and SMA bars as external structural bracing elements in low-rise shear walls [13]. Another application of SMAs has involved the shape memory effect to induce prestressing in concrete elements [14–19]. Other novel techniques have incorporated the combination of SMAs with fiber-reinforced polymers (FRPs), including superelastic SMA longitudinal bars in the plastic hinge region in beam–column joints coupled with FRP bars extending outside the critical zone [20], or exploiting the shape memory effect of SMAs to recovery permanent damage in beams prior to bonding FRP sheets to enhance strength [21].

Numerical modeling has also been employed to investigate the effect of SMAs on the behavior of precast segmental bridge piers [22] and overstrength and ductility of concrete buildings [23].

2. Research significance

This paper investigates the performance of concrete beams reinforced with superelastic SMA longitudinal bars to evaluate the applicability of SMAs as alternative reinforcement, and to provide benchmark tests against which constitutive models can be corroborated. This study includes the effect of loading (monotonic, cyclic, and reverse cyclic), assesses the energy dissipation and inelastic displacement recovery capacities, and discusses crack patterns, failure modes and hysteretic response. The beams and

SMA reinforcement are relatively larger in size and diameter, respectively, in comparison to previous investigations. The beams were tested to failure. Other studies attempted to salvage the SMA bars or limit damage to permit repairing and further testing. This paper also presents a preliminary constitutive model for superelastic SMAs based on linear unloading and reloading rules that considers accumulation of permanent straining and decaying of the unloading plateau stress, representing improvements to the frequently used flag-shaped model [24].

3. Properties of superelastic shape memory alloys

The ideal stress–strain response of superelastic SMAs for one reverse loading cycle is illustrated in Fig. 1. At low strains, typically not exceeding 1%, the response is linear elastic. Beyond the initial elastic region, the response substantially softens demonstrating nonlinearity followed by a near constant stress plateau. This is the result of stress-induced transformation from Austenite to Martensite and is known as forward transformation. At large strains, the material strain hardens due to the elastic response of the stress-induced Martensite state. The initial unloading response is linear followed by a sharp recovery of strains at almost constant stress. The latter characterizes the behavior of the material during the reverse transformation from Martensite back to Austenite. Finally, in the Austenite phase, the SMA returns to its original undeformed shape at zero stress.

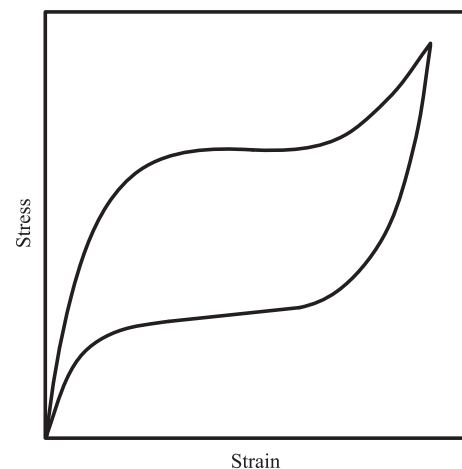


Fig. 1. Superelastic SMA stress–strain response.

4. Experimental program

An experimental program was conducted on seven simply supported reinforced concrete beams. The support and loading conditions of the beams were intended to promote a well-defined maximum moment location at midspan, which can be representative of maximum moment locations of other structural components. The beams were 2800 mm long (2400 mm from center to center of supports), 125 mm wide and 250 mm deep. The test variables included loading method and type of flexural reinforcement in the critical section. [Note: the critical section refers to the maximum moment location]. The specimens were named B1-SM, B2-SC, B3-SR, B4-NM, B5-NC, B6-NR, and B7-NCM. The letter S denotes conventional deformed reinforcing steel and N represents Nitinol (SMA). The letters M, C, and R denote the loading method: monotonic, cyclic, and reverse cyclic, respectively. Beams B1-SM, B2-SC, and B3-SR were the control specimens, while Beams B4-NM, B5-NC, and B6-NR were the companion Nitinol reinforced specimens.

An additional beam, B7-NCM, was constructed and tested to address deficiencies experienced during testing of Beams B4-NM and B5-NC. Beam B7-NCM was first tested under cyclic loading followed by monotonic loading in the opposite direction. For Beam B5-NC (cyclically loaded) the coupling connection between the SMA bar and the conventional deformed bar extending outside the critical region affected the strength, unloading response, and residual midspan displacements. The monotonic loading was also performed to better assess the response of an SMA reinforced beam controlled by failure in the critical section. This test complemented the results of Beam B4-NM, which failed outside the critical section, thus affecting the strength and ductility.

All beams were reinforced to promote a flexural response. Specimens B1-SM, B2-SC, B4-NM, and B5-NC were singly reinforced. Deformed longitudinal reinforcement in specimens B1-SM and B2-SC consisted of 10M bars, which have a nominal diameter of 11.3 mm and cross-sectional area 100 mm²; while 12.7 mm



Fig. 3. SMA and conventional reinforcement samples.

diameter Nitinol bars were used in the critical region of Beams B4-NM and B5-NC over a length of 600 mm centered at the midspan to optimize the material. The SMA bars were threaded at the ends and connected to 15M deformed steel (16 mm diameter and 200 mm² area) with threaded mechanical couplers. The larger bar area was used outside the critical section to prevent yielding of reinforcement outside this region. The standard threaded mechanical couplers were hexagon-shaped with an inner diameter of 12.6 mm, outer dimension of 22 mm, and approximate length of 50 mm, and provided a butt splice between the SMA and deformed bars. In addition, the Nitinol bars were reshaped to a diameter of 9.5 mm, as shown in Figs. 2 and 3, over a 300 mm length to promote yielding (forward transformation) and failure near the midspan and away from the threaded sections. Two additional bars were placed at the top of the beams that were subjected to reverse cyclic loading (B3-SR, B6-NR, and B7-NCM). For B3-SR, this consisted of 10M bars for the full length of the beam; while for B6-NR and B7-NCM, Nitinol coupled with 15M deformed bars were used. For the singly-reinforced beams (B1-SM, B2-SC, B4-NM, and B5-NC), two smooth 6.35 mm diameter detailing bars were placed at the top of the beams for the sole purpose of supporting the transverse shear reinforcement. The shear reinforcement, consisting of 6.35 mm diameter closed stirrups, was spaced at 100 mm along the entire length of the beams. A concrete clear cover of 20 mm was provided throughout. Note that the results for B5-NC are omitted herein due to the problems encountered during testing.

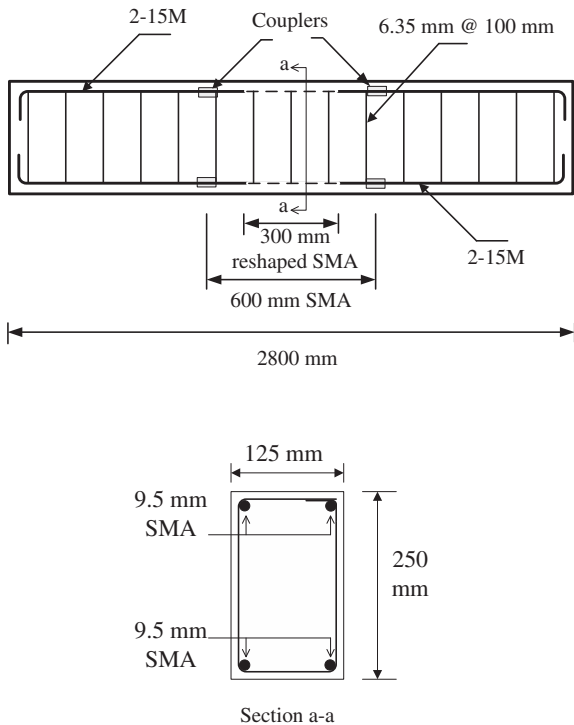
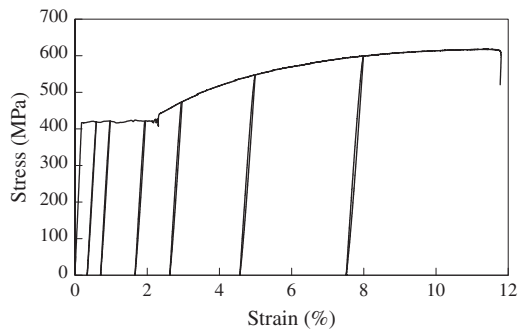


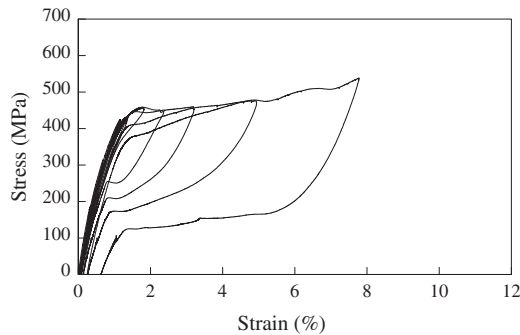
Fig. 2. Reinforcement details.

5. Material properties

The Nitinol bars had a nickel to titanium ratio of 0.56:0.44, and were heat treated to produce superelastic response at room temperature. Cyclic tension tests were performed on 300 mm long samples of each reinforcement type. The diameter of the Nitinol bars was reduced to 9.5 mm at mid-height and the ends were threaded and connected to conventional deformed 15M bars with threaded mechanical couplers to replicate the system used in the beams. The stress-strain responses of the 10M steel reinforcement and the Nitinol bars are illustrated in Fig. 4a) and b), respectively. Table 1 provides the yield and ultimate strengths, and elastic modulus. The Nitinol bar demonstrated a rounded loading curve;



(a)



(b)

Fig. 4. Cyclic stress–strain response: (a) 10M steel reinforcement; (b) SMA reinforcement.

Table 1
Reinforcement material properties.

Type	f_y (MPa)	f_u (MPa)	E_s (GPa)
6.35 mm	570	640	210
10M	425	615	205
15M	440	650	200
Nitinol	415	800	60

therefore, the yield point was based on a 0.2% offset, and the ultimate strength is based on specifications provided by the manufacturer. The residual strains provide a clear differentiation between the Nitinol and conventional deformed bars. During the last loading cycle, the Nitinol bar was strained to 7.7%, and upon unloading, the residual strain was 0.65%, representing a 91.6% strain recovery capacity. The conventional deformed 10M bar was subjected to a comparable strain of 8.0% during the last loading cycle. The resulting permanent strain was approximately 7.5%, representing a strain recovery of 6.25%.

The beams were constructed with normal-strength concrete with a target compressive strength of 30 MPa, 10 mm maximum aggregate size, and 100 mm slump. Table 2 provides the cylinder compressive strength and corresponding strain, and the initial tangent modulus on the day of testing for each beam type.

Table 2
Concrete material properties.

Beam type	f'_c (MPa)	E_c (GPa)	$\epsilon'_c \times 10^{-3}$
Conventional	34.6	31.4	2.45
SMA	32.7	28.4	2.52

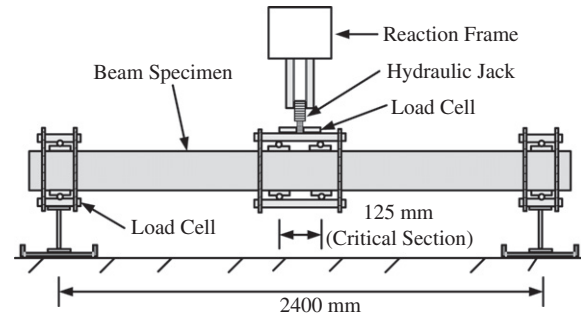


Fig. 5. Test setup.

5.1. Test setup and instrumentation

The specimens were tested using the setup shown in Fig. 5. All beams were tested under two central loads, spaced 125 mm apart, to ensure the midspan was subjected to constant flexure. Steel plates, 75 mm long, 150 mm wide, and 25 mm thick were positioned under each load to prevent local crushing of the concrete. The loading was applied by a hydraulic jack, mounted to a rigid steel assembly, and was measured by three load cells: one mounted under the hydraulic jack, and the other two at the supports. Deflection readings were continuously recorded at the midspan of the beams using two displacement cable transducers (DCT). The crack patterns, widths and spacing were recorded at each load stage. Loading was imposed in increments of 5 kN until failure for the monotonic tests, whereas displacement control was implemented for the cyclic tests following ATC-24 [25]. The initial loading corresponded to midspan displacements starting at $0.33\Delta_y$ to $1.0\Delta_y$ in increments of $0.33\Delta_y$, where Δ_y is the yield displacement. Thereafter, the loading was imposed in increments of Δ_y from $1.0\Delta_y$ until the end of testing. Each loading cycle consisted of a single repetition. Following ATC-24, the displacement at yield, Δ_y , is 1.33 times the displacement at first yield, which is defined as the displacement corresponding to 75% of the yield load, P_y . The yield loads (21 kN and 28 kN, respectively for the SMA and conventional reinforced beams) were determined from the experimental monotonic load–midspan displacement response and corresponded to the ordinate at the onset of yielding. Yield displacements, Δ_y , of 6.4 mm and 5.7 mm, respectively for the SMA and conventional reinforced beams, were calculated.

6. Test results

6.1. Cracking characteristics

For all beams, initial flexural cracking was observed, for the most part, in the critical region. Flexural cracking also developed outside the critical zone, and as the load increased, inclined shear cracks were noted near the supports. Additional shear cracks became evident with increased load, while the flexural cracking continued to propagate toward the loading points near the midspan of the beams. In both the conventional and SMA beams, the first flexural crack was observed at approximately 4 kN of load. At this load level, B1-SM (conventional, monotonic) and B4-NM (Nitinol, monotonic) had crack widths of 0.1 mm and 0.15 mm, respectively, in the critical zone. With increased load, the flexural cracks in the SMA beam became wider and were spaced farther in comparison to the conventional beam. This was attributed to the smooth surface of the Nitinol bars. At yielding, the flexural cracks in B1-SM were 0.35 mm wide and spaced approximately 100 mm; while in B4-NM, the cracks were 2.0 mm wide and spaced at 140 mm. Prior to failure, and at a displacement ductility of approximately $7\Delta_y$,

Table 3
Cracking characteristics.

Loading cycle	Beam							
	B2-SC $S_{cr} = 110$ mm		B7-NCM $S_{cr} = 155$ mm		B3-SR $S_{cr} = 100$ mm		B6-NR $S_{cr} = 150$ mm	
	W_{cr} (mm)	R_{cr} (mm)	W_{cr} (mm)	R_{cr} (mm)	W_{cr} (mm)	R_{cr} (mm)	W_{cr} (mm)	R_{cr} (mm)
1 Δ_y	0.3	0.21	1.8	0.28	0.28	0.15	1.8	0.15
2 Δ_y	3.5	2.5	6	0.32	1.5	1.25	5	0.4
3 Δ_y	4.5	3	11	1.1	2.5	2	9	0.8
4 Δ_y	5.5	4	16	2	3.5	2.75	12	1
5 Δ_y	6	5	24	2.4	5	4.25	21	2.5
6 Δ_y	7	5.5	34	3	8	6.4	30	3
7 Δ_y	–	–	–	–	9.5	7.5	48	5.5

S_{cr} = Crack spacing; W_{cr} = maximum crack width; R_{cr} = residual crack width.

Beam B1-SM experienced a maximum crack width of 11 mm, while a crack width of 52 mm was recorded for Beam B4-NM.

Table 3 provides the average crack spacing, maximum crack widths and residual crack widths for the beams tested under cyclic loads. At a displacement ductility of 1 Δ_y , conventional beams B2-SC and B3-SR recovered 30% and 46%, respectively, of the crack width opening. At 1 Δ_y , SMA Beams B7-NCM and B6-NR were capable of recovering approximately 84% and 92%, respectively, of the maximum crack widths. Prior to failure, and at a displacement ductility of 6 Δ_y for B2-SC and 7 Δ_y for B3-SR, the corresponding crack width recovery was approximately 21%. Conversely, at 6 Δ_y for B7-NCM and 7 Δ_y for B6-NR, the crack width recoveries were approximately 91% and 89%, respectively.

Fig. 6 illustrates the condition of the beams at the end of testing. Note that Fig. 6d) is a photo of Beam B7-NCM at the end of the cyclic loading phase.

6.2. Load–displacement response

Fig. 7a provides the load–displacement responses of Beams B1-SM, B4-NM, and B7-NCM, while Fig. 7b provides the normalized responses to account for the tensile yield force ($A_s f_y$) of the flexural reinforcement in the critical region. In addition, the midspan displacement is replaced by the displacement ductility to reflect the differences in yield displacement.

The conventional beam (B1-SM) failed at approximately 65 mm, corresponding to 36 kN of load, by concrete crushing in the flexural compression zone, after significantly yielding of the longitudinal reinforcement. Beam B4-NM failed at approximately 60 mm, corresponding to 28 kN due to rupturing of the Nitinol bar at the threaded section adjacent to the mechanical coupler. Concrete crushing in the flexural compression zone and a large flexural crack in the critical section were visible at failure. Note that B4-NM failed away from the critical section; therefore, the beam experienced less strength and ductility. Beam B7-NCM failed at approximately 80 mm or 34 kN of load by rupturing of the Nitinol bar in the critical section coinciding with concrete crushing in the flexural compression zone.

SMA Beam B4-NM had a similar elastic stiffness as B1-SM up to approximately 17 kN. Beyond this load level, there was softening in the response as the Nitinol bar experienced yielding (forward transformation). The post-yielding stiffness was comparable to B1-SM. The initial stiffness of Beam B7-NCM was less than both B1-SM and B4-NM mostly due to damage that was experienced by the beam during the cyclic loading phase. The post-yielding stiffness was similar to the other beams; however, Beam B7-NCM experienced a hardening response beyond 60 mm. Table 4 provides the yield and ultimate loads, and the ultimate displacement ductility. Fig. 7b demonstrates that the normalized yield load was similar for the beams. Beyond yielding, the SMA beams experienced

slightly larger normalized load capacity. Furthermore, Nitinol Beam B7-NCM experienced larger normalized load capacity at the end of testing.

The normalized load–displacement ductility responses of the Nitinol and conventional reinforced beams under cyclic and reverse cyclic loading are shown in Fig. 8a and b, respectively. The results indicate that the SMA and conventional reinforced beams experienced comparable normalized yield load, normalized ultimate load, and ductility. Testing of Beam B7-NCM was terminated prior to failure to permit monotonic loading in the opposite direction; therefore, the ultimate ductility was not realized. The unloading curves demonstrated a similar initial unloading stiffness; however, the SMA beams (B7-NCM and B6-NR) experienced a rapid recovery of displacement when the Nitinol bars reached the reverse transformation stress. Beams B2-SC and B3-SR failed in flexure by concrete crushing in the flexural compression zone, preceded by significant yielding of the longitudinal reinforcement. For Beam B7-NCM, a major crack was visible in the critical section prior to halting the test. Beam B6-NR failed due to rupturing of the Nitinol bar at the transition zone where the bar diameter changed from 12.7 mm to 9.5 mm, resulting in a reduction in the load-carrying capacity and ultimate ductility. Concrete crushing near the load application was also visible at failure.

7. Discussion of results

Fig. 9 provides the midspan displacement recovery capacities for the beams under cyclic and reverse cyclic loading. The SMA beam subjected to reverse cyclic loading demonstrated higher recovery capacity relative to the cyclically loaded SMA beam. The conventional reinforced beams demonstrated similar behavior. This difference was associated with the reduction of stiffness in the members due to damage experienced under load reversals. The conventional reinforced beams experienced a significant reduction in the capacity to recover inelastic deformations in comparison to the SMA reinforced beams. Under reverse cyclic loading, and at a displacement ductility of approximately 9.5, the SMA beam recovered 85% of the midspan displacement, while the conventional beam only realized a recovery of 26%. Under cyclic loading, the SMA and conventional reinforced beams recovered 80% and 17%, respectively, at a displacement ductility of 6.5. Fig. 9 highlights the progressive reduction in the re-centering capability of the conventional reinforced beams; a consequence of the linear unloading behavior of the reinforcement, which resulted in accumulation of permanent strains. The SMA beams, on the other hand, maintained a recovery capacity of approximately 75–100% for the ductility demands imposed during testing.

Fig. 10 provides the energy dissipation experienced by the beams subjected to cyclic and reverse cyclic loading at each displacement ductility level. In general, the SMA beam subjected to

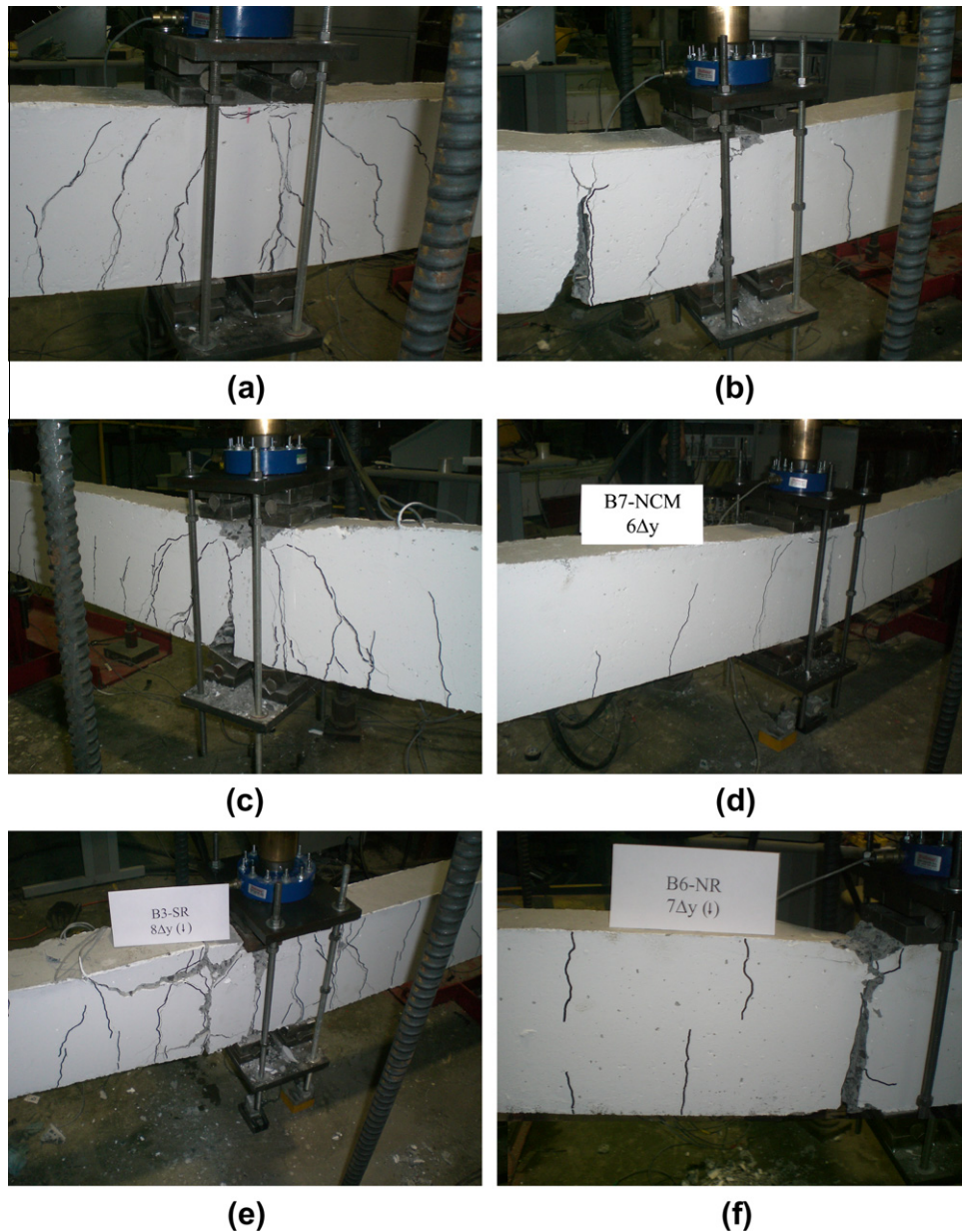


Fig. 6. Failure conditions of test beams: (a) B1-SM; (b) B4-NM; (c) B2-SC; (d) B7-NCM; (e) B3-SR; (f) B6-NR.

cyclic loading dissipated energy comparable to the conventional reinforced beam; whereas, the conventional reinforced beam dissipated significantly more energy than the SMA beam under reverse cyclic loading. At the ultimate displacement ductility under reverse cyclic loading, 3345 kN mm and 1205 kN mm of energy were dissipated by the conventional and SMA reinforced beams, respectively. Thus, the SMA beam dissipated approximately 36% of the energy dissipated by the conventional beam. This difference in energy dissipation is attributed to the flag shape response of the SMA bar under cyclic loading. Accounting for differences in yield displacement (ductility) and tensile yield force of the reinforcing bars, the SMA beam dissipated 46% of the energy dissipated by the conventional beam. If consideration is given to the location of failure in B6-NR at the transition zone, the difference in energy dissipation would further be reduced. The ultimate ductility for the beams under reverse cyclic loading was approximately 9.5. Referring to Fig. 7, the difference in SMA to conventional beam strength capacity was 1.165 at a displacement ductility of 9.5. Therefore, the energy dissipated by the SMA beam under reverse cyclic loading could reasonably be

54% of that dissipated by the conventional beam. This assumes that the monotonic response represents the backbone envelope for reverse cyclic loading.

8. Towards hysteretic modeling of SMA reinforced elements

A preliminary hysteretic constitutive model for superelastic SMA bars based on a uniaxial phenomenological approach was developed to be compatible with a compression field methodology. The proposed model was implemented into Program VecTor2 [26], a nonlinear two-dimensional finite element program applicable to concrete membrane structures. VecTor2 uses a smeared, rotating-crack formulation based on the Modified Compression Field Theory [27] and the Disturbed Stress Field Model [28]. The program algorithm is based on a secant stiffness formulation using a total-load iterative procedure. The program was previously updated to simulate the hysteretic response of reinforced concrete members [29–31].

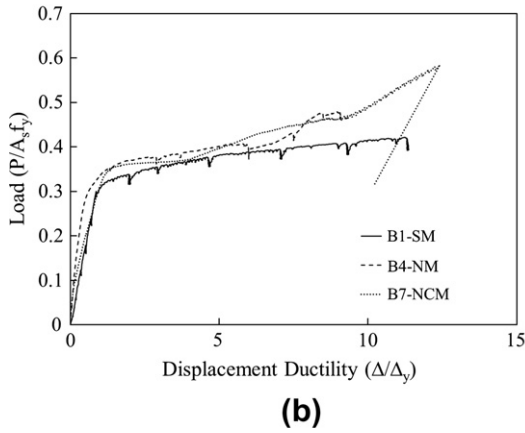
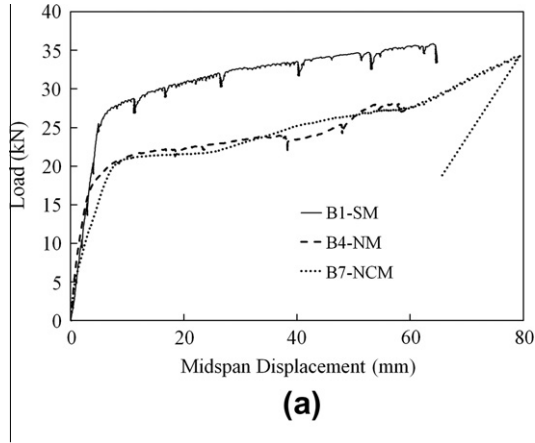


Fig. 7. Monotonic response: (a) load–displacement; (b) normalized load–displacement ductility.

Table 4
Load and displacement capacities.

Beam	Yield load		Ultimate load		Ductility
	Actual (kN)	Normalized	Actual (kN)	Normalized	
B1-SM	28	0.33	36	0.42	11.3
B2-SC	28	0.33	35	0.41	8.2
B3-SR	27	0.32	35	0.41	9.4
B4-NM	21	0.36	28	0.48	9.3
B6-NR	20	0.34	23	0.39	9.5
B7-NCM ^a	21	0.34	24	0.41	6.4
B7-NCM ^b	21	0.36	34	0.58	12.4

^a Results of the cyclic load test. This beam was not tested to failure.

^b Results of the monotonic test.

8.1. Superelastic SMA reinforcement model

The proposed model, as illustrated in Fig. 11, is based on a trilinear backbone envelope response, which is assumed to be identical to the monotonic response. The backbone includes: initial linear elastic loading; yielding (forward transformation); and strain hardening, which defines the stress-induced elastic response of Martensite. Improvements to other models [24,32–35] includes explicit consideration of permanent strains (Fig. 4b); the degradation of the lower plateau stress (reverse transformation), which results from the recovery of strains; and a trilinear unloading response. The backbone envelope response is described by the following formulations:

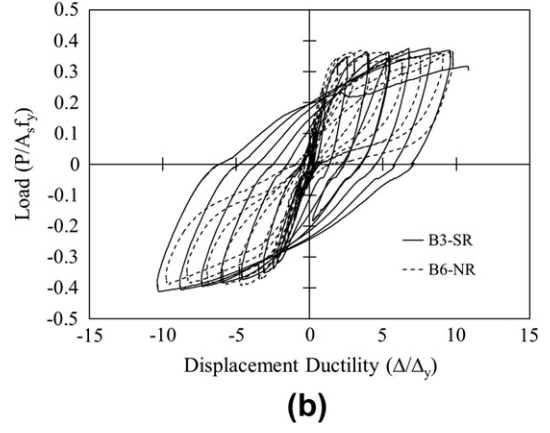
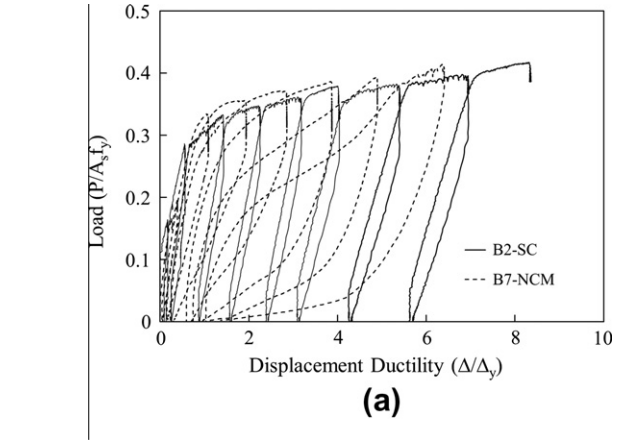


Fig. 8. Normalized load–displacement ductility responses: (a) cyclic loading; (b) reverse cyclic loading.

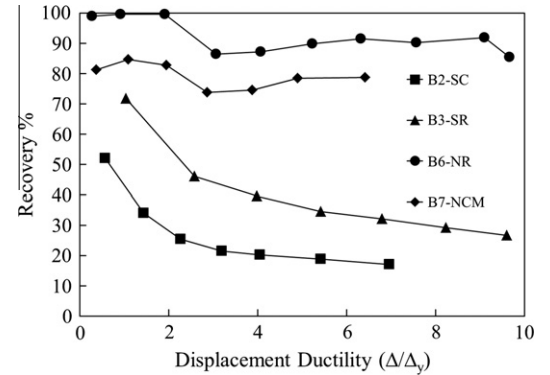


Fig. 9. Recovery capacity–displacement ductility behaviours.

$$f_s = f_{s-i} + E_i(\epsilon_s - \epsilon_{s-i}) \quad 0 < \epsilon_s < \epsilon_y \quad (1)$$

$$f_s = f_y \quad \epsilon_y < \epsilon_s < \epsilon_{sh} \quad (2)$$

$$f_s = f_{s-i} + E_{sh}(\epsilon_s - \epsilon_{s-i}) \quad \epsilon_{sh} < \epsilon_s < \epsilon_u \quad (3)$$

where f_s is the stress at the current strain state ϵ_s , f_{s-i} and ϵ_{s-i} are the stress and strain from the previous load step, respectively, f_y is the yield stress, E_i is the initial modulus of elasticity, E_{sh} is the strain hardening modulus, ϵ_y and ϵ_u are the yield and ultimate strains, respectively, and ϵ_{sh} is the strain at the onset of strain hardening. From coupon testing or specifications provided by the manufacturer, f_y , E_i , E_{sh} , ϵ_y , ϵ_u , and ϵ_{sh} can be determined. The same formulations apply for SMA reinforcement in tension or compression.

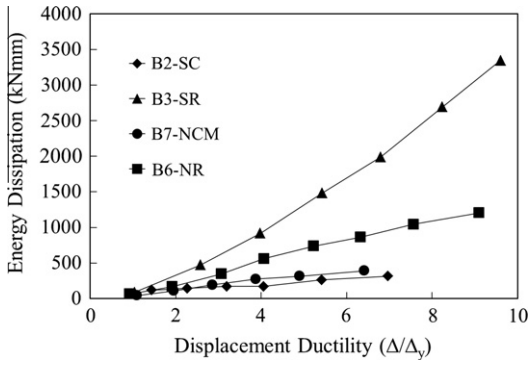


Fig. 10. Energy dissipation–displacement ductility responses.

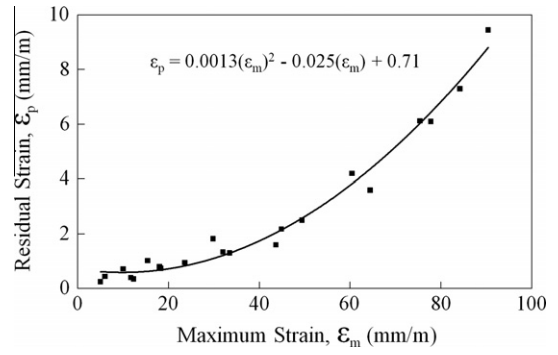


Fig. 12. Plastic offset strain.

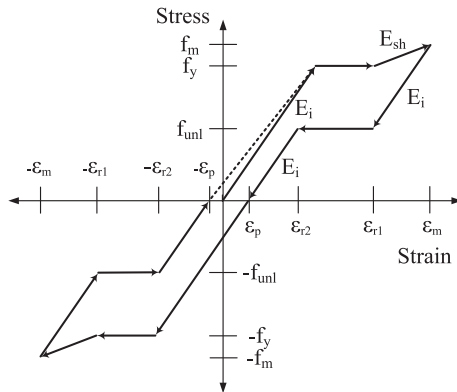


Fig. 11. SMA plastic offset constitutive model.

The unloading response includes: initial unloading, unloading plateau stress, and unloading to the plastic offset strain. The unloading branches can be described by the following formulations:

$$f_s = f_{s-i} + E_i(\epsilon_s - \epsilon_{s-i}) \quad \epsilon_{r1} < \epsilon_s < \epsilon_m, \epsilon_p < \epsilon_s < \epsilon_{r2} \quad (4)$$

$$f_s = f_{unl} \quad \epsilon_{r2} < \epsilon_s < \epsilon_{r1} \quad (5)$$

where ϵ_{r1} and ϵ_{r2} are the first and second unloading strains, respectively, ϵ_m is current maximum strain, ϵ_p is the plastic offset strain, and f_{unl} is the unloading plateau stress that defines the reverse transformation from Martensite to Austenite. The unloading modulus, E_i , is set equal to the initial modulus as per Eq. (1). Relationships for ϵ_p , ϵ_{r1} , and f_{unl} were derived as functions of the current maximum strain using stress–strain data obtained from tensile coupon testing of SMA bars conducted in this study:

$$\epsilon_p = 0.0013(\epsilon_m)^2 - 0.025(\epsilon_m) + 0.71 \quad (6)$$

$$\epsilon_{r1} = 0.86(\epsilon_m) - 0.45 \quad (7)$$

$$f_{unl}/f_y = -0.006(\epsilon_m) + 0.73 \quad (8)$$

The first unloading strain ϵ_{r1} was defined as the strain corresponding to the intersection between initial unloading as per Eq. (4) and the unloading plateau stress. The unloading plateau stress f_{unl} was identified as the stress corresponding to zero stiffness along the unloading path. The second unloading strain, ϵ_{r2} , is implicitly determined within the program from the intersection of the unloading plateau stress and the unloading to plastic offset (Eq. (4)). Figs. 12–14 illustrate the strong correlation between the above parameters and the maximum strain. The plastic offset strain data is well captured by a quadratic formulation, while the first unloading strain and the unloading plateau stress are

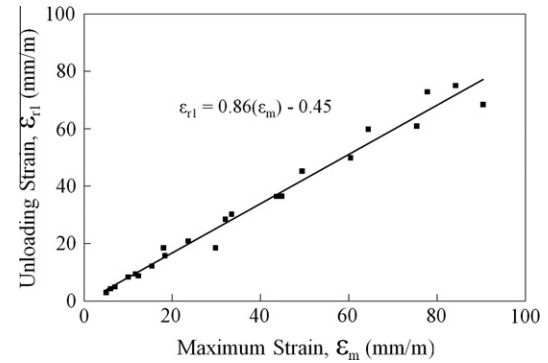


Fig. 13. First unloading strain.

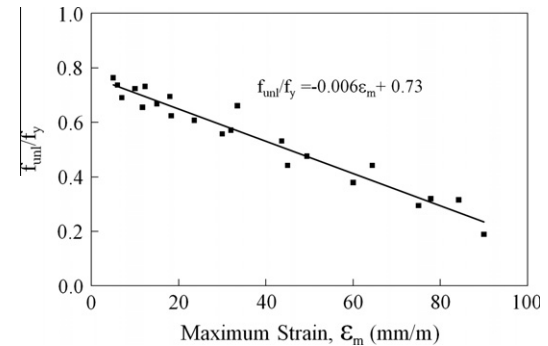


Fig. 14. Unloading plateau stress.

represented by simple linear relationships. Note that f_{unl} is normalized with respect to the yield stress to eliminate the influence of stress on the formulation.

The reloading response, following a full cycle, is linear originating from the plastic offset strain ϵ_p to the yield strain ϵ_y . Thereafter, the response follows the backbone envelope curve.

8.2. Finite element analysis

Analyses were conducted using VecTor2 on the cyclically loaded SMA reinforced beams to assess the proposed SMA hysteretic model. Fig. 15 provides a schematic of the finite element mesh developed for the beams. Rectangular plane stress elements were used to represent the concrete, truss bar elements were used to model the longitudinal reinforcement and the transverse shear reinforcement was smeared within the concrete elements. A total of 1008 rectangular elements were used for the concrete and 224 truss elements for the top and bottom longitudinal reinforcement.

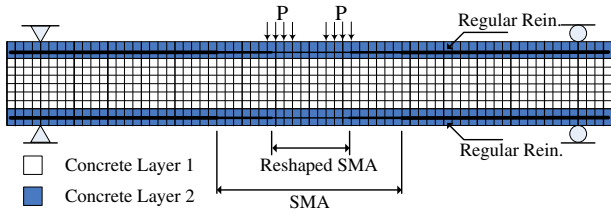


Fig. 15. Finite element mesh for SMA beams.

Two different concrete types were used due to varying reinforcement ratios. One was assigned to the concrete elements between the top and bottom longitudinal reinforcement and contained smeared reinforcement in the vertical direction to account for shear reinforcement. The two concrete layers adjacent to the longitudinal reinforcement were assigned to the second concrete type. These elements contained smeared reinforcement in the vertical direction due to the stirrups and smeared reinforcement in the out-of-plane direction to account for the legs of the stirrups. The latter explicitly accounts for the confining effect near the edges of the beams due to the closed stirrups.

The longitudinal 15M steel reinforcement and SMA bars (Fig. 2) were modeled using discrete, two-nodded truss bar elements. The threaded couplers were represented by a truss bar with the same length, material properties, and cross sectional area as the couplers. The 15M bars and the couplers were assumed perfectly bonded to the surrounding concrete. Bond-slip elements were used at the interface of the SMA truss elements and the rectangular concrete elements to model the bond characteristics of the smooth SMA. The default materials models of VecTor2 [26] were selected for the analysis of the beams. The only exception was the proposed SMA hysteretic model. The loading was applied as imposed displacements following the same protocol that was used during testing.

Fig. 16 shows the experimental and numerical responses of Beam B7-NCM. In general, the analysis reasonably simulated the behavior observed during testing. The numerical yield and ultimate strengths of 20.4 kN and 26.5 kN, respectively, were only 7% and 9% greater than experimentally recorded. The residual deformations upon unloading were accurately modeled. The unloading curves were well simulated at early stages of loading. With increased loading, discrepancies are evident. The initial unloading response was better simulated than the unloading plateau stress. The analysis was terminated at approximately 40 mm of midspan displacement and was not pushed to failure, which was consistent with testing.

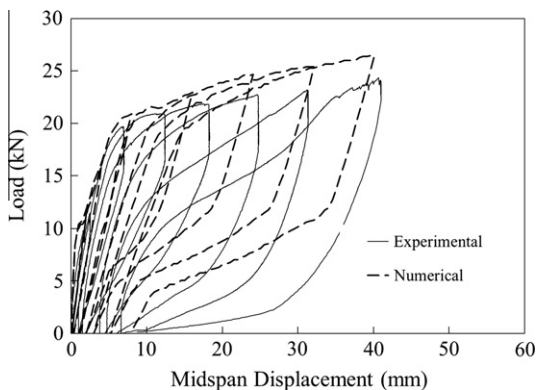


Fig. 16. Numerical and experimental load-displacement responses for beam B7-NCM.

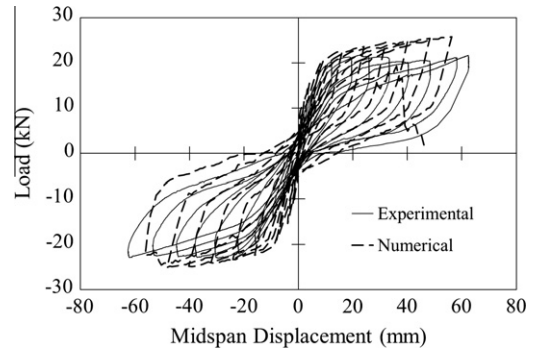


Fig. 17. Numerical and experimental load-displacement responses for beam B6-NR.

Fig. 17 provides the experimental and numerical responses of Beam B6-NR. The hysteretic behavior was well simulated, including peak strength, ductility, residual deformations, and unloading response. The numerical yield strength of 18 kN was 9% greater than experimentally recorded; whereas, the analysis provided an ultimate load of 25.7 kN, which was 20% higher than experimentally observed. The simulated failure mode was controlled by rupturing of the SMA at the transition zone, which was consistent with that observed during testing.

To further assess the proposed SMA model, the numerical and experimental responses for the experimentally recorded peak strength for Beam B6-NR are shown in Fig. 18. The numerical response satisfactory simulated the response. The analysis established a load of 24.5 kN, while the corresponding value recorded during testing was 21.6 kN. The numerical energy dissipation at this load level was 737 kN mm which is only 11% greater than the experimental dissipated energy of 668 kN mm.

To demonstrate the applicability of the preliminary constitutive SMA model, an analysis was conducted on a large-scale SMA reinforced beam-column joint tested by Youssef et al. [12]. Superelastic SMA bars were used in the plastic hinge region of the beam. The column and beam were 3000 mm and 1630 mm in length, respectively. Both members had identical cross-section dimensions (250 mm wide and 400 mm deep). 2–20M longitudinal bars (nominal diameter of 19.5 mm and cross-sectional area of 300 mm²) were placed at the top and bottom of the beam and column, while closed 10M ties were provided at different spacing in the members. Screw-lock mechanical couplers were used to couple the 20 mm diameter SMA to the 20M deformed steel bars extending beyond the plastic hinge region into the beam and joint. The total length of SMA bars was 450 mm (measured from center to center of the couplers). Fig. 19 provides details of the reinforcement.

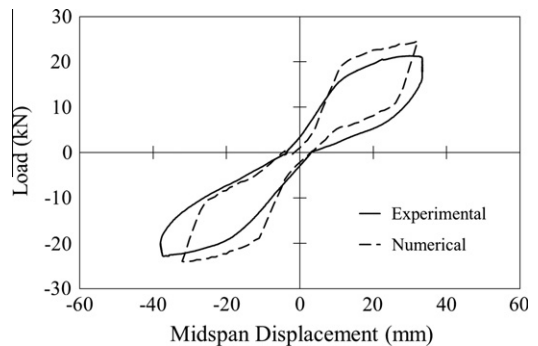


Fig. 18. Numerical and experimental peak strength responses for beam B6-NR.

The top and the bottom of the column were pin connected to a loading frame. The specimen was subjected to a constant axial load applied of 350 kN at the top of the column and incremental reverse cyclic vertical displacements at the tip of the beam. Two repetitions of loading were applied at each displacement level. Testing was terminated at a beam tip displacement of 72 mm.

The finite element model of the beam–column joint (Fig. 20) consisted of seven concrete layers. Three layers were used to represent the column and joint, and four layers were used for the beam. The concrete properties were similar in all the layers; however, the reinforcement ratio of the smeared transverse ties in these layers varied. The concrete layer adjacent to the longitudinal reinforcement also contained smeared reinforcement in the out-of-plane direction to account for the legs of the stirrups.

The longitudinal reinforcement in the beam and column was modeled with perfectly bonded truss bars. The couplers were represented by a truss bar with equivalent length, material properties and cross sectional area. The finite element mesh consisted of 1008 plane stress rectangular elements to represent the concrete layers and 232 truss bar elements to model the longitudinal reinforcement. In addition, bond–slip elements were used to model the bond between the SMA smooth bars and the surrounding concrete. The column axial loading and beam tip vertical displacements followed the same loading protocol as used during testing.

The numerical and experimental results are shown in Fig. 21. In general, the SMA hysteretic model satisfactorily simulated the experimental response in terms of stiffness, strength, ductility, and displacement recovery. The pre-yielding stiffness was slightly overestimated in the analysis. The numerical yield strength was 37.5 kN; an over prediction of approximately 14% in the positive direction of loading. The post-yield stiffness was comparable to the recorded response and the peak load captured in the analysis was 72 kN, which was only 6% greater than recorded (68 kN) in the positive direction of loading. There was slightly more discrepancy between the numerical yield and ultimate strengths relative to those recorded during testing in the negative direction of loading; however, the general response was still well simulated. The plastic deformations were slightly underestimated by the analysis. At the end of the testing, the numerical and experimental residual displacements were 6.1 mm and 9.8 mm, respectively. The experimental unloading response was nearly linear and the reverse transformation plateau was not as evident as in the analysis. These discrepancies were probably due to the slippage of the SMA bars inside the couplers during testing.

In general, the proposed preliminary model consisting of a series of linear segments provided reasonable simulations demonstrating the applicability of the model and VecTor2 to model SMA reinforced members. Improved simulation results can be

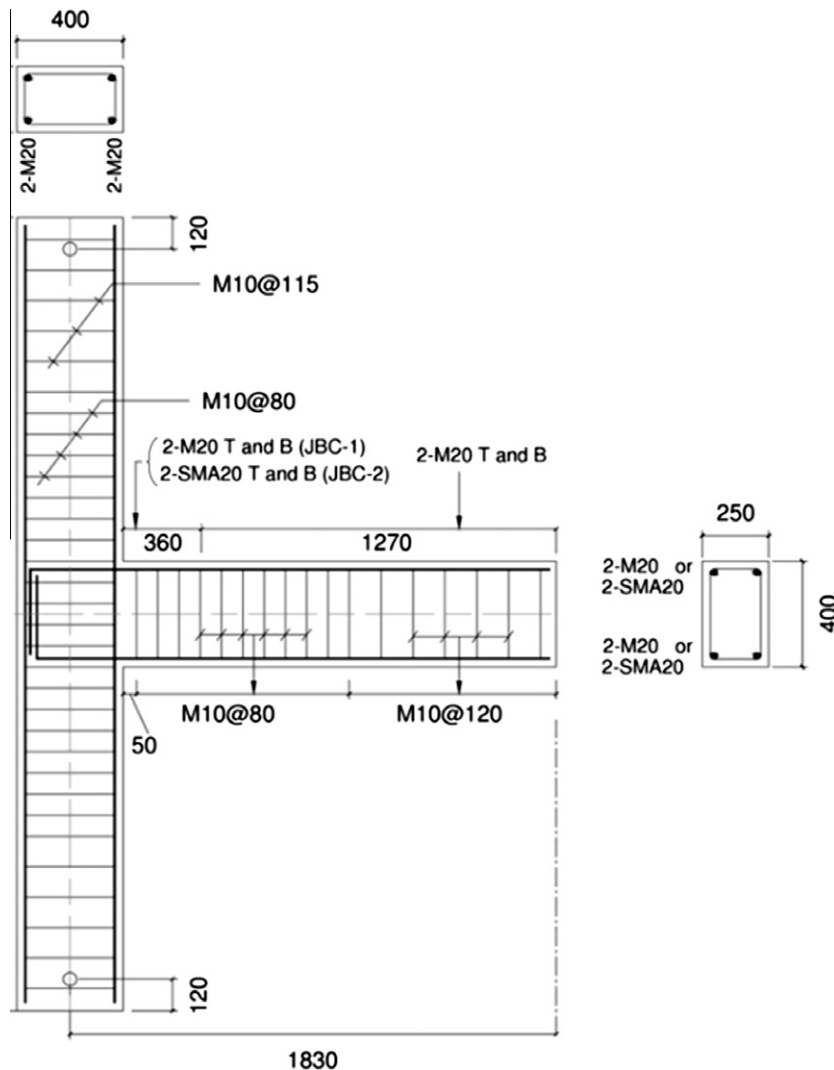


Fig. 19. Details of beam–column joint specimen JCB2 [36].

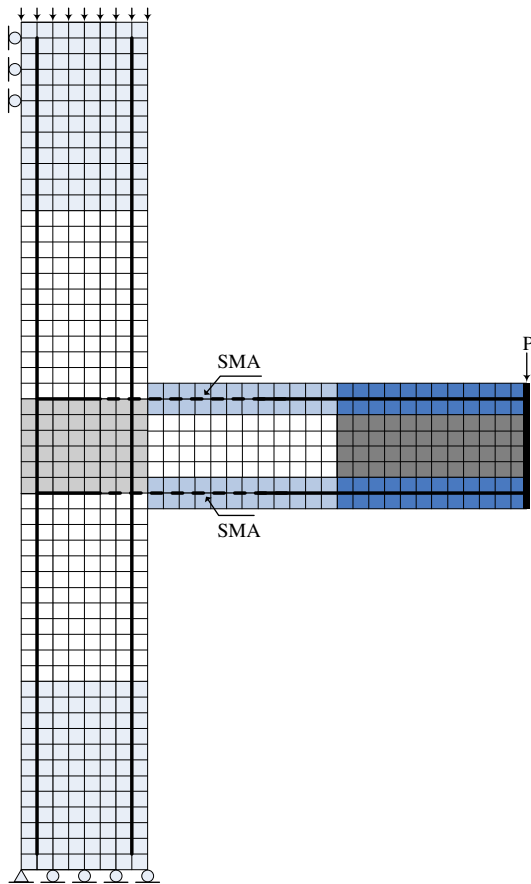


Fig. 20. Finite element mesh for SMA beam–column joint JCB2.

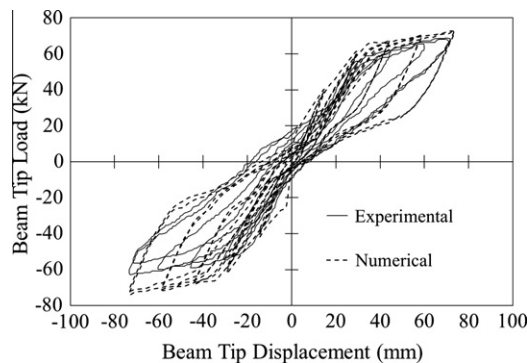


Fig. 21. Numerical and experimental [36] load–displacement responses for SMA beam–column joint JCB2.

achieved with nonlinear unloading and reloading rules. In addition, a reloading response that aims for the previous maximum strain will improve the hysteretic response. Furthermore, with additional coupon testing of SMA bars, the plastic offset strain ϵ_p , the first unloading strain ϵ_{r1} and the unloading plateau stress f_{unt} formulations can be updated.

9. Conclusions

This study focused on a well-defined testing program of flexure-critical SMA reinforced beams subjected to monotonic, cyclic, and reverse cyclic loading. In addition, a linear, plastic offset hysteretic constitutive model for superelastic SMA compatible with a

compression field approach was proposed. The following specific conclusions are drawn:

1. Large superelastic Nitinol bars used in larger-scale concrete beams perform similar to smaller-scale SMA reinforced members indicating consistency and reliability of SMAs.
2. Nitinol was superior to the conventional deformed steel at limiting residual displacements and crack widths in the concrete beams.
3. Nitinol reinforced beams experienced higher normalized yield and ultimate loads in comparison to the conventional reinforced beams, provided the Nitinol bars did not rupture at the threaded ends near the mechanical couplers or at the transition zone.
4. The SMA beams sustained comparable displacement ductility to conventional reinforced beams.
5. The SMA beam, under cyclic loading, dissipated energy comparable to the conventional reinforced beam. However, under reverse cyclic loading, the SMA reinforced beam dissipated approximately 54% of the energy dissipated by the conventional reinforced beam.
6. Threaded couplers used to connect Nitinol bars with deformed bars should be located a sufficient distance from the critical region to avoid failure of the Nitinol bar at the location of the coupler.
7. The preliminary plastic offset SMA hysteretic constitutive model consisting of a trilinear backbone envelope curve and linear segments to simulate unloading and reloading was successfully implemented into Program VecTor2. The model was capable of modeling the force–displacement response of the SMA reinforced beams and an SMA reinforced beam–column joint.
8. A notable deficiency in the proposed model was the unloading response with increased loading. Future refinements in the model, including nonlinear unloading will provide improved simulations.

In summary, the capacity to recover inelastic displacements, exhibit yielding and strain hardening, while sustaining large displacement ductility are structural characteristics that make superelastic SMAs an appealing alternative reinforcement for structural applications.

Acknowledgements

The research program was funded by Public Works and Government Services Canada (PWGSC), and the Canadian Seismic Research Network (CSRN). The authors wish to express their gratitude to both organizations.

References

- [1] DesRoches R, McCormick J, Delemont M. Cyclic properties of superelastic shape memory alloy wires and bars. *J Struct Eng, ASCE* 2004;130(1):38–46.
- [2] Tyber J, McCormick J, Gall K, DesRoches R, Maier HJ, Maksoud AEA. Structural engineering with NiTi I: basic materials characterization. *J Eng Mech, ASCE* 2007;133(9):1019–29.
- [3] McCormick J, Tyber J, DesRoches R, Gall K, Maier HJ. Structural engineering with NiTi II: mechanical behaviour and scaling. *J Eng Mech, ASCE* 2007;133(9):1019–29.
- [4] Dolce M, Cardone C. Mechanical behavior of shape memory alloys for seismic applications – 2. Austenite NiTi wires subjected to tension. *Int J Mech Sci* 2001;43:2657–77.
- [5] Alam MS, Youssef MA, Nehdi M. Utilizing shape memory alloys to enhance the performance and safety of civil infrastructure: a review. *Can J Civ Eng* 2007;34(9):1075–86.
- [6] Janke L, Czaderski C, Motavalli M, Ruth J. Applications of shape memory alloys in civil engineering structures – overviews, limits and new ideas. *Mater Struct* 2005;38:578–92.

- [7] Song G, Ma N, Li HN. Applications of shape memory alloys in civil structures. *Eng Struct* 2006;128:1266–74.
- [8] Deng Z, Li Q, Sun H. Behaviour of concrete beam with embedded shape memory alloy wires. *Eng Struct* 2006;28:1691–7.
- [9] Saiidi MS, Sadrossadat-Zadeh M, Ayoub C, Itani A. Pilot study of behaviour of concrete beams reinforced with shape memory alloys. *J Mater Civil Eng, ASCE* 2007;19(6):454–61.
- [10] Saiidi MS, Wang H. Exploratory study of seismic response of concrete columns with shape memory alloys reinforcement. *ACI Struct J* 2006;103(3):436–43.
- [11] Saiidi MS, O'Brien M, Sadrossadat-Zadeh M. Cyclic response of concrete bridge columns using superelastic nitinol and bendable concrete. *ACI Struct J* 2009;106(1):69–77.
- [12] Youssef M, Alam M, Nehdi M. Experimental investigation on the seismic behaviour of beam–column joints reinforced with superelastic shape memory alloys. *J Earthquake Eng* 2008;12:1205–22.
- [13] Effendy E, Liao W, Song G, Mo Y, Loh C. Seismic behaviour of low-rise shear walls with SMA bars. *Earth & space 2006: engineering, construction, and operations in challenging environment, Houston, TX; 2006*. p. 1–8.
- [14] Maji AK, Negret I. Smart prestressing with shape memory alloy. *J Eng Mech, ASCE* 1998;124(10):1121–8.
- [15] El-Tawil S, Ortega-Rosales J. Prestressing concrete using shape memory alloy tendons. *ACI Struct J* 2004;101(6):846–51.
- [16] Krstulovic-Opara N, Naaman AE. Self-stressing fiber composites. *ACI Struct J* 2000;97(2):335–44.
- [17] Shin M, Andrawes B. Lateral cyclic behavior of reinforced concrete columns retrofitted with shape memory spirals and FRP wraps. *J Struct Eng* 2011;137(11):1282–90.
- [18] Shin M, Andrawes B. Experimental investigation of actively confined concrete using shape memory alloys. *Eng Struct* 2010;32(3):656–64.
- [19] Choi E, Chung YS, Choi JH, Kim HT, Lee H. The confining effectiveness of NiTiNb and NiTi SMA wire jackets for concrete. *Smart Mater Struct* 2010;19(3):8.
- [20] Nehdi M, Alam MS, Youssef MA. Development of corrosion-free concrete beam column joint with adequate seismic energy dissipation. *Eng Struct* 2010;32(9):2518–28.
- [21] Li H, Liu ZQ, Ou JP. Experimental study of a simple reinforced concrete beam temporarily strengthened by SMA wires followed by permanent strengthening with CFRP plates. *Eng Struct* 2008;30(3):716–23.
- [22] Roha H, Reinhorn AM. Hysteretic behavior of precast segmental bridge piers with superelastic shape memory alloy bars. *Eng Struct* 2010;32(10):3394–403.
- [23] Alam MS, Moni M, Tesfamariam S. Seismic overstrength and ductility of concrete buildings reinforced with superelastic shape memory alloy rebar. *Eng Struct* 2012;34:8–20.
- [24] Auricchio F, Sacco E. A superelastic shape-memory-alloy beam model. *J Intell Mater Syst Struct* 1997;8(6):489–501.
- [25] ATC. ATC-24, guidelines for cyclic seismic testing of components of steel structures. Redwood City, CA: Applied Technology Council; 1992. 57pp.
- [26] Wang PS, Vecchio FJ. VecTor2 and formworks user's manual. Canada: Department of Civil Engineering, University of Toronto; 2002.
- [27] Vecchio FJ, Collins MP. The modified compression-field theory for reinforced concrete elements subjected to shear. *ACI J* 1986;83(3):219–31.
- [28] Vecchio FJ. Disturbed stress field mode1 for reinforced concrete: formulation. *ACI Struct J* 2000:1070–7.
- [29] Palermo D, Vecchio FJ. Simulation of cyclically loaded concrete structures based on the finite element method. *ACSE J Struct Eng* 2007;133(5):728–38.
- [30] Palermo D, Vecchio FJ. Compression field modeling of reinforced concrete subjected to reversed loading: verification. *ACI Struct J* 2004;101(2):155–64.
- [31] Palermo D, Vecchio FJ. Compression field modeling of reinforced concrete subjected to reversed loading: formulation. *ACI Struct J* 2003;100(5):616–25.
- [32] Ren W, Li H, Song G. A one-dimensional strain-rate dependent constitutive model for superelastic shape memory alloys. *Smart Mater Struct* 2000:191–7.
- [33] Graesser J, Cozzarelli A. Shape-memory alloys as new materials for a seismic isolation. *J Eng Mech* 1991:2590–608.
- [34] Andrawes B, DesRoches R. Sensitivity of seismic applications to different shape memory alloy models. *J Eng Mech* 2008:173–83.
- [35] Zak A, Cartmell M, Ostachowicz W, Wiercigroch M. One-dimensional shape memory alloy models for use with reinforced composite structures. *Smart Mater Struct* 2003:38–346.
- [36] Alam SM, Youssef MA, Nehdi M. Analytical prediction of the seismic behaviour of superelastic shape memory alloy reinforced concrete elements. *Eng Struct* 2008;30(12):3399–411.